

基于光频域反射差分相位解调的分布式折射率传感

花培栋, 丁振扬*, 刘琨, 郭浩晗, 张腾, 李胜, 刘骥, 江俊峰, 刘铁根

天津大学精密仪器与光电子工程学院, 光电信息技术教育部重点实验室, 天津市光纤传感工程中心, 天津 300072

摘要 提出一种基于光频域反射(OFDR)差分相位解调的拉锥光纤分布式折射率传感方法。首先, 理论分析了差分相位解调方法的原理并仿真计算了相位随外界折射率变化的灵敏度特性。实验中利用平均去噪与小波平滑实现了 $340\text{ }\mu\text{m}$ 传感空间分辨率的分布式折射率传感解调, 其中有效传感区域的长度为 45 mm , 相位与外界折射率变化的线性拟合度为0.997, 各折射率下的最大标准差为 0.0067 rad , 灵敏度为 1328.6 rad/RIU , 接近仿真结果 1483.7 rad/RIU 。与互相关解调方法相比, 差分相位解调方法的线性拟合度与标准差均较优, 且传感空间分辨率提升了10倍。这种基于差分相位的解调方式为实现微米级分布式生物传感提供了思路。

关键词 光纤光学; 分布式光纤传感; 折射率传感; 光频域反射技术; 差分相位解调; 拉锥光纤

中图分类号 TP212 文献标志码 A

DOI: 10.3788/AOS231941

1 引言

光纤折射率(RI)传感器由于具有高精度、高灵敏度、抗电磁干扰、耐腐蚀、成本低、易制备等优势, 在生化传感、环境监测等领域受到研究人员的广泛关注^[1-3]。目前, 常见的光纤折射率传感器主要包括表面等离子体共振传感器^[4]、局部表面等离子体共振传感器^[5]、光纤布拉格光栅^[6]、长周期光纤光栅^[7]、光纤回音壁模式^[8]、光纤法布里-珀罗传感器^[9]、光子晶体光纤^[10]、D型光纤^[11]、拉锥光纤^[12]、超材料传感器^[13]、损失模共振传感器^[14]等。然而, 绝大多数光纤折射率传感器属于分立式单点传感器, 无法实现多点探测甚至分布式传感。

光频域反射技术(OFDR)基于对光纤瑞利后向散射谱(RBS)的检测, 具有测量精度高、传感空间分辨率高、测量距离长等优势^[15-16]。瑞利后向散射是由沿光纤的随机折射率波动引起的, 可被视为具有随机周期的长而弱的光纤布拉格光栅。当外界折射率发生变化时, OFDR系统中的待测光纤(FUT)传感区域的局部RBS会产生光学频移。这个频移可以利用测量组RBS和参考组RBS之间的局部互相关来表征, 最终获得分布式折射率传感结果。分布式折射率传感不仅能够获得溶液折射率的大小, 还能局部检测溶液的扩散过程、测试流体的分布, 这些都是分立式传感器甚至准分布式传感器无法实现的。2017年, Du等^[17]首次提出一种基于OFDR中RBS偏移和宏观弯曲光纤的分布

式折射率传感器, 通过将一根单模光纤(SMF)弯曲到曲率半径仅有几毫米, 实现了在 $1.3348\sim1.3557$ 范围的分布式折射率测量, 传感空间分辨率为 4 cm , 灵敏度约为 20 nm/RIU 。Xu等^[18]也通过弯曲一根标准SMF来激发穿透周围介质的高阶模, 研制出一种基于高性能OFDR的分布式折射率传感器, 通过将SMF弯曲到 4 mm 的半径, 实现了 2 mm 传感空间分辨率下 39.08 nm/RIU 的折射率灵敏度测量。但是这类基于宏观弯曲纤维的方法只能感测在FUT上制造的弯曲结构的位置, 依旧难以实现对局部溶液折射率变化的监测。Sypabekova等^[19]提出一种基于刻蚀高散射MgO基纳米颗粒掺杂SMF的OFDR分布式折射率传感器, 其传感空间分辨率为 1 mm , 但折射率灵敏度仅为 1.53 nm/RIU 。Zhu等^[20]提出一种使用刻蚀多芯光纤的温度补偿分布式折射率传感器, 利用OFDR对刻蚀多芯光纤进行检测, 实现了 19 cm 传感长度和 5.3 mm 传感空间分辨率下宽至 $1.33\sim1.44$ 感测范围的折射率测量, 并在 1.44 折射率附近获得 47 nm/RIU 的最大灵敏度。Fu等^[21]提出并演示了一种基于刻蚀锗掺杂SMF的光频域反射分布式光纤折射率传感器, 实现了 10 cm 传感长度、 5.25 mm 传感空间分辨率下 $1.33\sim1.44$ 折射率传感范围内约为 757 GHz/RIU (6.056 nm/RIU)的平均折射率灵敏度检测。拉锥光纤具有强倏逝场、易制备等特点, 是一种优秀的折射率传感器^[22]。因此, 被拉锥至一定长度的光纤非常适用于局部监测的分布式折射率传感。Ding

收稿日期: 2023-12-15; 修回日期: 2024-01-23; 录用日期: 2024-02-05; 网络首发日期: 2024-02-20

基金项目: 国家重点研发计划(2023YFF0715700)、国家自然科学基金(61975147)

通信作者: *zyding@tju.edu.cn

等^[23]提出一种在OFDR中使用拉锥细径光纤的分布式折射率传感器,基于拉锥光纤具有大的倏逝场耦合和模间干涉效应,实现了4.25 mm传感空间分辨率下62.52 nm/RIU的折射率灵敏度测量,并在最后利用甘油溶液测试了甘油扩散过程中的折射率变化,验证了该传感器的分布式折射率传感能力。

传统OFDR分布式折射率传感利用互相关解调算法,具有良好的抑噪能力与稳定性,但很难实现微米级传感空间分辨率的分布式折射率测量,因此目前这类基于互相关解调的分布式折射率传感尚不足以应用到分布式生物分析、药物设计等领域^[24]。与互相关解调方法不同,基于差分相对相位解调的OFDR通过感知RBS的相对相位变化来实现传感。实际测量中每一个采集的数据点均能够实现对相对相位变化的感知,因此基于差分相位解调的OFDR有望实现理论传感空间分辨率检测^[25-27]。然而,目前基于差分相位OFDR的报道集中于应变传感的研究^[28-31]。

本文提出一种基于OFDR差分相位解调方式的分布式折射率传感方法。首先,理论分析了基于差分相位折射率传感的原理,并仿真计算了相位变化随外界折射率变化的灵敏度特性。其次,在实验中通过均值滑窗与小波平滑,实现了340 μm传感空间分辨率下1.334761~1.334983折射率范围内的分布式传感。实验中传感器为拉锥细径光纤,拉锥后光纤总长140 mm,有效传感区域为45 mm,传感区域的锥腰半径为6 μm。然后,对相位变化与外界折射率变化进行线性拟合,其线性拟合度为0.997,各个折射率下的最大标准差为0.0067 rad,灵敏度为1328.6 rad/RIU。实验测量灵敏度与仿真结果(1483.7 rad/RIU)接近。最后,对所提出的差分相位解调法与传统互相关解调算法进行比较,发现差分相位解调法的传感空间分辨率提升了10倍,其线性拟合度与测量标准差均优于互相关解调算法。

$$\frac{d\Delta\phi(z)}{dz} = -\frac{4\pi}{c} [n_1(z) \cdot \delta f + \delta n(z) \cdot f_{01}] - \frac{4\pi z}{c} \left[\frac{\delta f \cdot dn_1(z)}{dz} + f_{01} \cdot \frac{d\delta n(z)}{dz} \right] + \frac{d\Delta\varphi(z)}{dz} = \\ -\frac{4\pi}{c} \left[n_1(z) \cdot \delta f + \delta n(z) \cdot f_{01} - z \cdot \delta f \cdot \frac{dn_1(z)}{dz} - z \cdot f_{01} \cdot \frac{d\delta n(z)}{dz} \right] + \frac{d\Delta\varphi(z)}{dz} \quad (4)$$

在实际测量中, $n_1(z)$ 的波动很小,因此 $\frac{dn_1(z)}{dz} \approx 0$ 。

假设拉锥光纤传感区域的表面光滑且均匀,外界折射率变化是一致的, $\delta n(z)$ 远大于它沿传感区域的变化率 $\frac{d\delta n(z)}{dz}$ 。因此,式(4)可以用 $\delta n(z) f_{01} \gg z f_{01} \frac{d\delta n(z)}{dz}$

进行简化:

$$\frac{d\Delta\phi(z)}{dz} \approx -\frac{4\pi}{c} [n_1(z) \cdot \delta f + \delta n(z) \cdot f_{01}] + \frac{d\Delta\varphi(z)}{dz} \quad (5)$$

2 理论分析与方法

由于差分相位的解调方式是直接测量由外界折射率变化引起的相对相位变化,相较于传统互相关解调方式更加灵敏,因此这种解调方法有望实现微米级的分布式折射率传感。下面将介绍基于差分相位的OFDR折射率传感原理。通过OFDR测量的参考组与测量组信号的相对差分相位^[30]可以表示为

$$\Delta\phi(z) = 2\pi\tau_1 f_{01} - 2\pi\tau_2 f_{02} + \varphi_1(\tau_1) - \varphi_2(\tau_2), \quad (1)$$

式中: f_{01} 和 f_{02} 分别表示参考组和测量组信号的初始光频率, $f_{02} = f_{01} + \delta f$ 表示由激光器波动与采集卡触发误差引起的初始光频波动; $\varphi_1(\tau_1) - \varphi_2(\tau_2)$ 表示由扫频激光器引起的参考信号与测量信号的非线性残余噪声; $\tau_1 = \frac{2n_1(z)z}{c}$ 、 $\tau_2 = \frac{2n_2(z)z}{c}$ 分别表示参考组与测量组信号在拉锥光纤传感区域的时间延迟, z 表示传感区域的任意位置, c 为真空中的光速, $n_1(z)$ 和 $n_2(z)$ 分别表示系统测量臂中待测拉锥光纤在外界折射率发生变化前后的有效折射率。在外界折射率发生变化后,参考组和测量组中探测臂待测光纤的有效折射率之间的关系为

$$n_2(z) = n_1(z) + \delta n(z), \quad (2)$$

式中: $\delta n(z)$ 表示外界折射率变化时参考组与测量组中传感区域的折射率分布差异。将式(2)代入 τ_1 和 τ_2 并代入式(1)后,式(1)可以简化为

$$\Delta\phi(z) = -\frac{4\pi z}{c} [n_1(z) \cdot \delta f + \delta n(z) \cdot f_{01}] + \Delta\varphi(z), \quad (3)$$

式中: $\Delta\varphi(z) = \varphi_1(\tau_1) - \varphi_2(\tau_2)$ 。从式(3)可以看出,忽略初始光频波动与激光器非线性噪声,外界折射率变化引起的 $\delta n(z)$ 为参考组与测量组信号相对相位改变的主要原因。为了测量沿拉锥光纤传感区域的相对相位局部变化,对式(4)进行微分处理,得到

在式(5)中, $n_1(z)$ 和 f_{01} 可视为定值, $\frac{d\Delta\varphi(z)}{dz}$ 为噪声项, δf 为初始光频波动,因此 $\frac{d\Delta\phi(z)}{dz}$ 的变化主要来源于 $\delta n(z)$ 。对于OFDR系统,输出端的参考臂和测量臂上各个位置的拍频信号可以表示为

$$I = I_1 + I_2 + 2\sqrt{I_1 I_2} \cos[\Delta\Phi(z)], \quad (6)$$

式中: I_1 和 I_2 分别表示参考臂信号和测量臂信号的光强; $\Delta\Phi(z)$ 表示测量臂与参考臂不同位置的相位差。在OFDR系统中,测量臂上待测光纤的位置决定了

参考臂和测量臂之间的光程差。因此,当外界折射率无变化时,参考臂和测量臂之间的相位差可以表示为

$$\Delta\Phi_1(z) = \frac{2\pi f_{01}}{c} \cdot n_1(z) \cdot 2z_1, \quad (7)$$

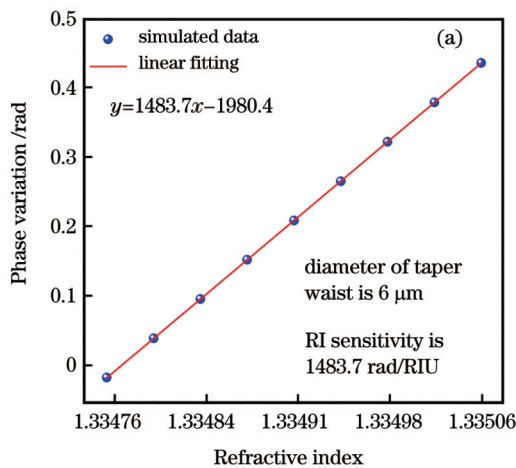
式中: z_1 表示待测光纤的位置。当外界折射率发生变化时,拉锥光纤处发生的模间干涉会导致测量臂中有有效折射率发生变化并引起RBS频移^[23]。因此,外界折射率变化后,参考臂和测量臂之间的相位差可以表示为

$$\Delta\Phi_2(z) = \frac{2\pi(f_{01} - \Delta f)}{c} \cdot n_2(z) \cdot 2z_2. \quad (8)$$

式中: r 表示拉锥光纤的锥腰半径; n_{SRI} 表示外界溶液的初始折射率。通过式(11)可以计算出光频移动与外界折射率变化量的关系,从而反推出外界折射率变化时对应的光频变化。

3 数值仿真

基于式(11),可以通过设定频移量 Δf 来确定对应频移量下的外界折射率变化量 Δn_{SRI} ,由此得到外界折射率变化时的频移灵敏度 $S_{\text{SRI}} = \Delta f / \Delta n_{\text{SRI}}$,再由 S_{SRI} 反推出外界折射率变化后的光频移动量。将上述光频移动量代入式(10)即可得出相位变化随外界折射率变化的理论数值。下面通过数值计算表征外界折射率变化时对应的相位变化。初始参数设置为 $f_{01} = 1.9723 \times 10^5$ GHz(初始波长为1520 nm)、 $n_1(z) = 1.444$,并设



在折射率变化前后OFDR拍频的同一共振波长位置,有 $\Delta\Phi_1 = \Delta\Phi_2$ 。而外界折射率的变化不会引起待测拉锥光纤轴向位置的变化,因此 $z_2 = z_1$ 。结合式(2)、式(7)和式(8)可化简得到:

$$\Delta n(z) = -\frac{\Delta f}{f_{01} - \Delta f} \cdot n_1(z). \quad (9)$$

由于 $f_{01} \gg \Delta f$,将式(9)代入式(5)并化简可得:

$$\frac{d\Delta\phi(z)}{dz} \approx -\frac{4\pi}{c} \left[n_1(z) \cdot \delta f - n_1(z) \cdot \Delta f \right] + \frac{d\Delta\varphi(z)}{dz}. \quad (10)$$

结合之前的研究^[23],RBS频移 Δf 与外界折射率变化 Δn_{SRI} 的关系可以表示为

$$\Delta n_{\text{SRI}} = \sqrt{n_1^2(z) - \left\{ c(f_{01} - \Delta f) \left/ \left[\pi r f_{01}^2 \ln \left(\frac{f_{01} - \Delta f}{f_{01}} \right)^2 + \frac{c f_{01}}{\sqrt{n_1(z)^2 - n_{\text{SRI}}^2}} \right] \right\}^2} - n_{\text{SRI}}, \quad (11)$$

定每次外界折射率变化时模间干涉引起的测量臂光频移动 $\Delta f = 14$ GHz。为了表征差分相位解调法的理论灵敏度并与实验结果对比,仿真了6 μm时相位变化与外界折射率变化的关系。其中外界初始折射率为 $n_{\text{SRI}} = 1.334761$,每次变化量 $\Delta n_{\text{SRI}} = 0.000037$,变化范围为1.334761~1.335057。仿真结果如图1(a)所示,斜率1483.7 rad/RIU即为理论的测量灵敏度。从式(11)可以看出, Δf 与拉锥光纤的锥腰半径 r 有关,因此通过上述参数可以仿真外界折射率变化时的理论测量灵敏度与拉锥光纤锥腰直径的关系,结果如图1(b)所示。当外界折射率变化时,测量灵敏度会随着拉锥光纤锥腰直径的增加而减少。因此在未来的研究中,可以通过减小拉锥光纤的锥腰直径来提升测量的灵敏度。

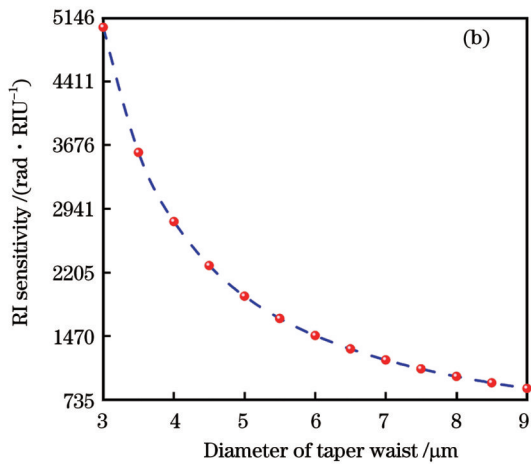


图1 相位变化灵敏度数值仿真结果。(a)不同外界折射率下相对于初始外界折射率的相对相位变化数值仿真结果;(b)外界折射率变化时不同锥腰直径下的相位变化灵敏度数值仿真结果

Fig. 1 Numerical simulation results of phase variation sensitivity. (a) Numerical simulation results of phase variations under different external RI; (b) numerical simulation results of phase variation sensitivity in different diameters of taper waist when external RI changes

4 实验研究与讨论

4.1 实验装置与过程

基于OFDR分布式折射率传感的实验装置如图2所示。实验中可调谐激光器(TLS; TLB-8800, Newports, INC.)的调谐范围为1510 GHz(12 nm), 调谐速率为 1×10^4 GHz/s(80 nm/s), 激光器发射激光的初始波长为1520 nm。使用小的扫频范围是为了降低相位噪声的影响。来自TLS的光通过1:99的保偏耦合器分至附加干涉仪和主干涉仪。1%的光进入附加迈克耳孙干涉仪。该干涉仪提供一个外部时钟来触发数据采集, 以实现对主干涉信号进行等距光频率采样。附加干涉仪的延迟光纤长136 m。两个法拉第旋转镜可以使附加干涉仪对偏振不敏感。99%的光进入主马赫-曾德尔干涉仪后, 再通过20:80的保偏

耦合器将光分至参考臂与测量臂, 其中80%的光进入待测光纤后经瑞利后向散射返回环形器。待测光纤为拉锥光纤, 总长度为14 cm, 锥腰直径为6 μm ^[24]。最后使用偏振分集探测器在干涉仪中分别接收参考臂信号和测量臂的瑞利后向散射信号, 这可以有效地消除偏振衰落效应^[32]。实验测量氯化钠(NaCl)溶液折射率的变化。考虑到未来的应用环境为生物液体环境, 因此实验中测试质量浓度范围为0.88~1.00 g/mL(生理盐水的质量浓度范围)的NaCl溶液, 对应的折射率范围为1.334761~1.334983。首先, 将光纤浸入500 mL质量浓度为1.00 g/mL的NaCl溶液中, 并加入去离子水来稀释NaCl溶液, 每次稀释的质量浓度变化为0.02 g/mL, 对应0.000037的折射率变化。考虑到溶液中的扩散过程, 实验数据的测量时间间隔为2 min。

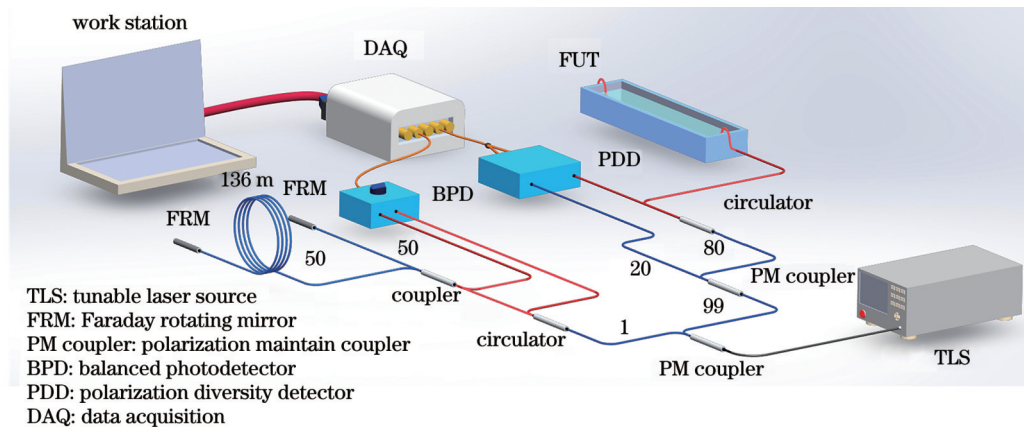


图2 基于OFDR分布式折射率传感实验装置示意图

Fig. 2 Experimental setup for distributed optical fiber RI sensing using tapered fibers in OFDR

4.2 测量步骤与结果

结合测量理论与实验过程, 基于差分相位解调的OFDR信号处理过程如图3所示。具体的信号处理过程如下:

步骤1: 在初始状态下运行OFDR系统, 一次获得参考组的拍频时域信号。在加入去离子水稀释等待2 min后, 再次运行系统获取测量组的拍频时域信号。

步骤2: 利用快速傅里叶变换(FFT)将参考组信号和测量组信号从时域实信号转换为空间域复信号。

步骤3: 取参考组和测量组复信号的相角项即可分别获取参考组和测量组信号在空间域每个位置的相位项。幅值项对应于距离域, 用于快速找到待测光纤的传感区域以便获取传感区域的相位, 这能减少不必要的数据处理过程。传感区域内参考组与测量组信号各自的相位如图4(a)、(b)所示, 传感区域的距离域信号如图4(c)所示。

步骤4: 将步骤3中参考组与测量组信号传感区域的相位项作差分处理, 即可获得参考组与测量组信号

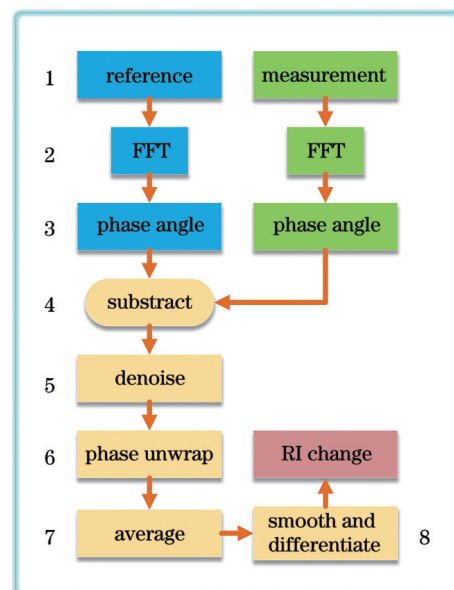


图3 基于差分相位解调方式的OFDR信号处理过程示意图

Fig. 3 Schematic of OFDR signal processing based on differential phase demodulation method

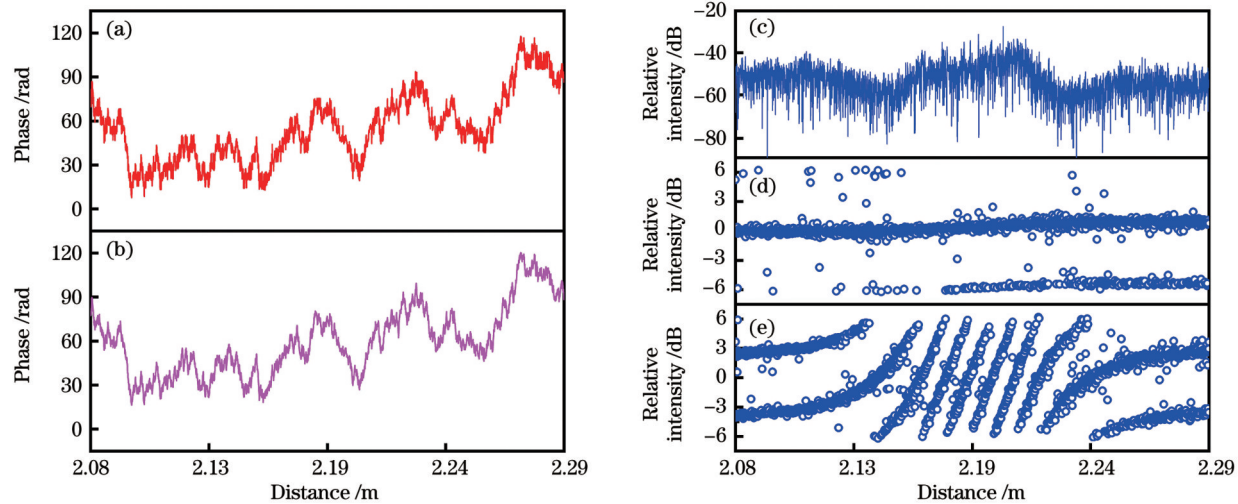


图 4 外界折射率变化前后传感区域的相对相位示意图。(a)参考组信号相位;(b)测量组信号相位;(c)拉锥光纤传感区域的距离域信号;(d)外界折射率变化前参考组与测量组信号的相对相位;(e)外界折射率变化后参考组与测量组信号的相对相位

Fig. 4 Schematic of relative phase in the sensing area before and after changes in external RI. (a) Phase of reference signal; (b) phase of measurement signal; (c) distance domain signal in the sensing region of tapered fiber; (d) relative phase between reference and measurement signals before external RI change; (e) relative phase between reference and measurement signals after external RI change

的相对相位 $\Delta\phi(z)$ 。图 4(b)、(c) 分别展示了外界折射率变化前后传感区域的相对相位。在外界折射率发生变化前, 参考组与测量组信号的相对相位保持相对平稳; 在外界折射率发生变化后, 参考信号与测量信号的相对相位在传感区域均匀变化。

步骤 5: 对相对相位 $\Delta\phi(z)$ 进行去噪处理以消除

相位噪声对后续相位解缠绕的影响。如果在步骤 4 后直接对 $\Delta\phi(z)$ 进行相位解缠绕处理, 由激光器初始光频差与相位噪声引起的波动将会引发图 5(a) 所示的相位跳变, 导致相位解缠绕出现错误。因此, 在相位解缠绕前需要进行去噪处理以消除引起相位跳变的噪声点。本文使用半径去噪方法抑制相位噪声^[28]。

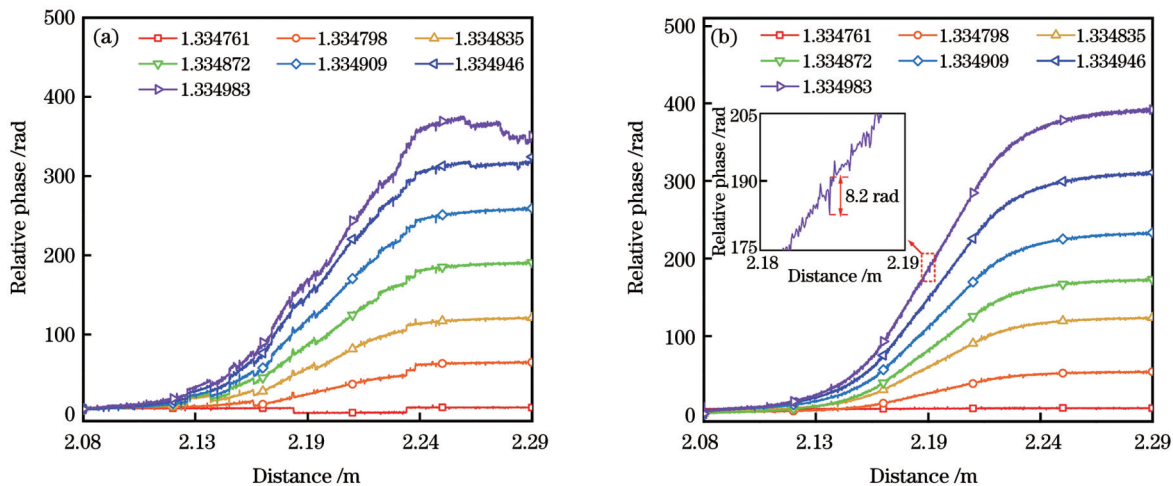


图 5 半径去噪前后的相对相位解缠绕曲线。(a)未进行半径去噪时的相对相位解缠绕曲线;(b)半径去噪后的相对相位解缠绕曲线,其插图为去噪后相位解缠绕曲线中的局部相位波动

Fig. 5 Relative phase unwrapping curves before and after radius denoising. (a) Relative phase unwrapping curves without radius denoising; (b) relative phase unwrapping curves with radius denoising, and the inset shows local phase noise in the phase unwrapping curve after denoising

步骤 6: 对步骤 5 去噪后的 $\Delta\phi(z)$ 进行相位解缠绕处理, 结果如图 5(b) 所示。可以清晰地看到, 经过去噪, 由噪声导致的相位解缠绕偏差得到了很好的抑制, 不同折射率下的相对相位在传感区域呈现出均匀的变

化。从图 5(b) 的插图可以发现, 测量结果仍然存在较大的相位波动, 因此需要进行平滑处理。

步骤 7: 对步骤 6 后 $\Delta\phi(z)$ 的相位解缠绕结果进行平均滑窗处理。将相位解缠绕结果分为若干段包含 H

个数据点的数据,计算每段数据中 H 个数据点的平均值以实现均值去噪。然而,平均滑窗过程将会降低OFDR传感的空间分辨率。OFDR系统的传感空间分辨率 ΔX 可以表示为

$$\Delta X = H \cdot \Delta Z, \quad (12)$$

式中: $\Delta Z = c/(2n \cdot \Delta F)$ 为OFDR系统中每个数据点对应的传感空间分辨率; n 为待测光纤的折射率; ΔF 为激光器的扫频范围。由于该实验的扫频范围为1510 GHz,因此这里的 $\Delta Z=68 \mu\text{m}$ 。**图6(a)**展示了340 μm 传感空间分辨率下($H=5$)拉锥光纤传感区域相位随距离的变化。可以看出,即使是通过平均滑窗进行均值滤波,340 μm 传感空间分辨率下传感区域折射率变化所引起的相位变化仍然无法区分。这种偏差来源于**图5(b)**插图中的相位噪声。因此,需要对步骤7平均滑窗后的数据进行进一步的平滑处理。

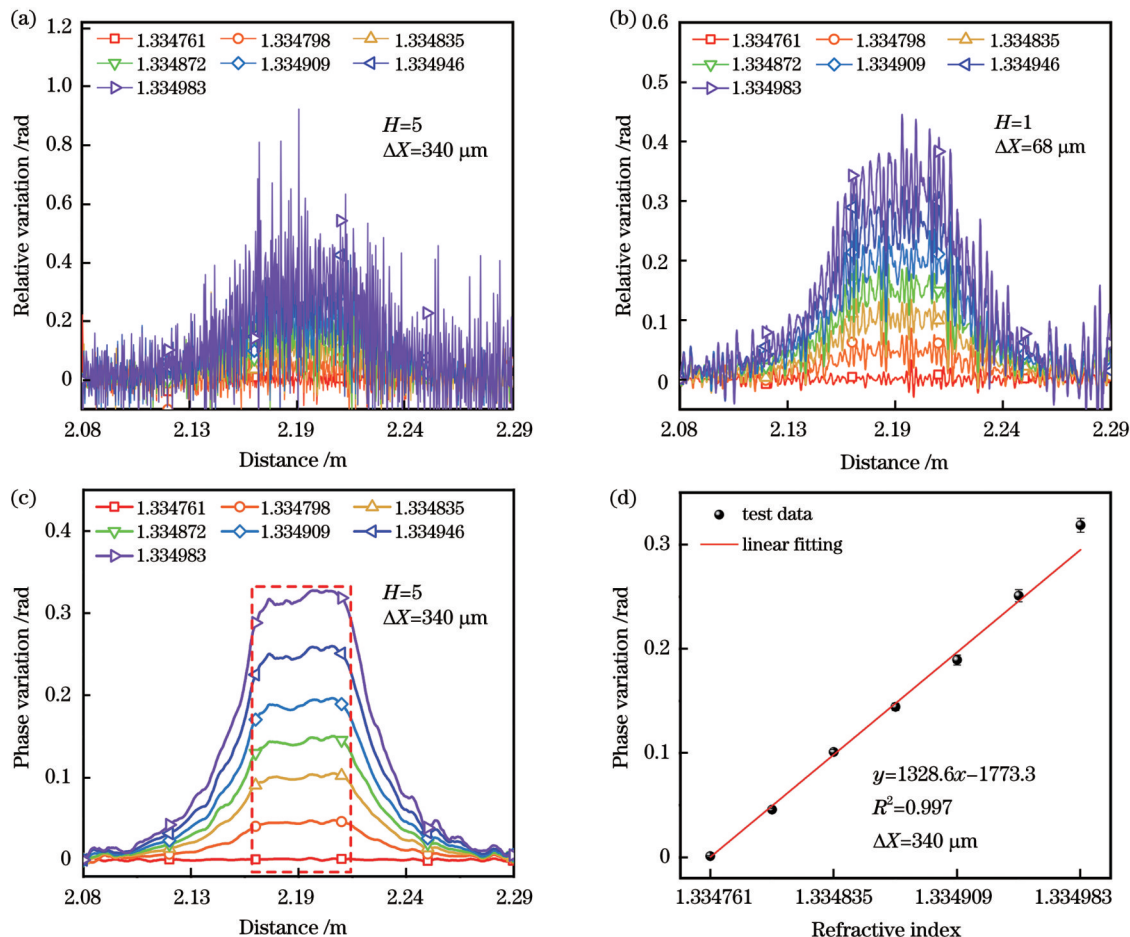
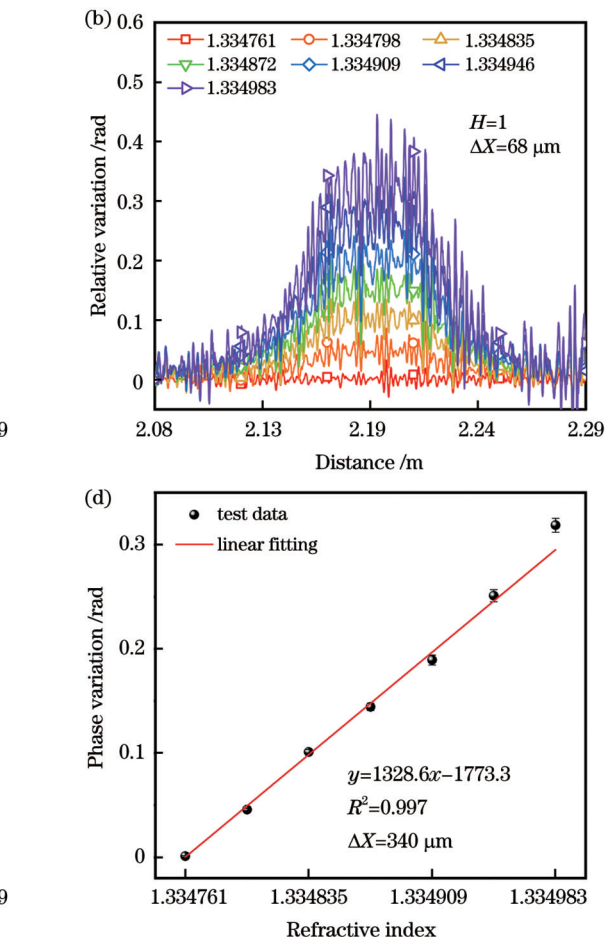


图6 拉锥光纤传感区域相位随距离的变化。(a)仅平均去噪,且传感空间分辨率为340 μm 时,不同折射率下相位随距离的变化;(b)仅小波去噪,且传感空间分辨率为68 μm 时,不同折射率下相位随距离的变化;(c)平均去噪并经过小波去噪后,传感空间分辨率为340 μm 时不同折射率下相位随距离的变化,其中红色方框表示拉锥光纤中心传感区域,长度为45 mm,锥腰直径为6 μm ;(d)平均去噪并经过小波去噪后,340 μm 传感空间分辨率下相位变化与外界折射率变化的线性拟合结果

Fig. 6 Variations in phase with distance in the tapered fiber sensing region. (a) Phase as a function of distance at different RI only with average denoising when $\Delta X=340 \mu\text{m}$; (b) phase as a function of distance at different RI only with wavelet denoising when $\Delta X=68 \mu\text{m}$; (c) phase as a function of distance at different RI with both average denoising and wavelet denoising when $\Delta X=340 \mu\text{m}$, and the red dashed box corresponds to central sensing region of tapered fiber, with length of 45 mm and taper waist diameter of 6 μm ; (d) after average denoising and wavelet denoising, linear fitting curve between phase and RI when $\Delta X=340 \mu\text{m}$

步骤8:对步骤7的结果进行小波平滑去噪并进行微分处理,得到外界折射率变化时相位随待测光纤位置的变化。由于绝大多数生物环境下的待测因子均在微米级甚至纳米级,因此实现微米级的分布式折射率传感是未来实现微米级分布式生物传感的基础。使用Daubechies小波族^[33]对步骤7平均滑窗后的数据进行进一步的平滑处理。平滑后的相对相位 $\Delta\phi(z)$ 经过微分处理后即可得到相位随待测光纤距离的变化。**图6(b)**展示了仅使用小波去噪时,即68 μm 传感空间分辨率($H=1$)下拉锥光纤传感区域相位随距离的变化。可以看到,在小波去噪后,68 μm 传感空间分辨率下传感区域折射率变化引起的相位变化已经能够区分,但是由于**图5(b)**插图中的相位噪声过大,传感区域的解调信号仍存在较大的波动。经过平均去噪($H=5$)且进行小波去噪后,在340 μm 传感空间分辨



率下,相位波动噪声能够得到很好的抑制,此时能够清晰地分辨出不同折射率下相位沿光纤距离变化的曲线,结果如图 6(c)所示。其中拉锥光纤的有效传感区域为中间 45 mm 范围,如图 6(b)的红框区域所示。在有效传感区域内传感灵敏度具有一致性,这是因为基于拉锥工艺,锥区中间 45 mm 范围的锥腰直径均可视为 6 μm ,而在红框左右范围外,锥腰直径逐渐增大,传感灵敏度快速下降。为了保证传感的一致性,仅考虑中间的分布式传感有效区域。图 6(d)展示了有效传感区域相位变化与外界折射率变化的线性拟合结果,线性拟合度为 0.997,各折射率下的最大标准差为 0.0067 rad,平滑后的测量灵敏度为 1328.6 rad/RIU。图 6(d)的实验测量灵敏度与图 1(b)的仿真结果 1483.7 rad/RIU 接近,其中的偏差主要来源于式(10)中初始光频 δf 与相位噪声 $\frac{d\Delta\phi(z)}{dz}$ 的影响。

4.3 与传统互相关解调方法的对比

为了比较所提出的差分相位解调方法与传统互

相关解调方法的差异,对图 6 的数据进行互相关解调^[15,34],结果如图 7 所示。图 7(a)展示了 340 μm 传感空间分辨率下利用互相关解调的拉锥光纤传感区域 RBS 随距离的变化。可见,340 μm 传感空间分辨率下互相关算法无法区分折射率的变化。通过设定不同的传感空间分辨率,最终在 340 μm 传感空间分辨率的可测量条件下,标定了不同外界折射率下待测光纤 RBS 随距离的变化,结果如图 7(b)所示。同样,对拉锥光纤有效传感区域 RBS 移动以及外界折射率变化进行线性拟合,结果如图 7(c)所示。线性拟合度为 0.995,各折射率下的最大标准差为 5.08 GHz,测量灵敏度为 3.043×10^5 GHz/RIU。与互相关解调方法相比,差分相位解调方法的线性拟合度更高。对比图 6(d)与图 7(c)的误差棒,明显看出平滑后的差分相位解调方法的标准差低于互相关解调方法。更重要的是,相较于互相关解调方法,差分相位解调方法的传感空间分辨率提升了 10 倍,达到了百微米量级。

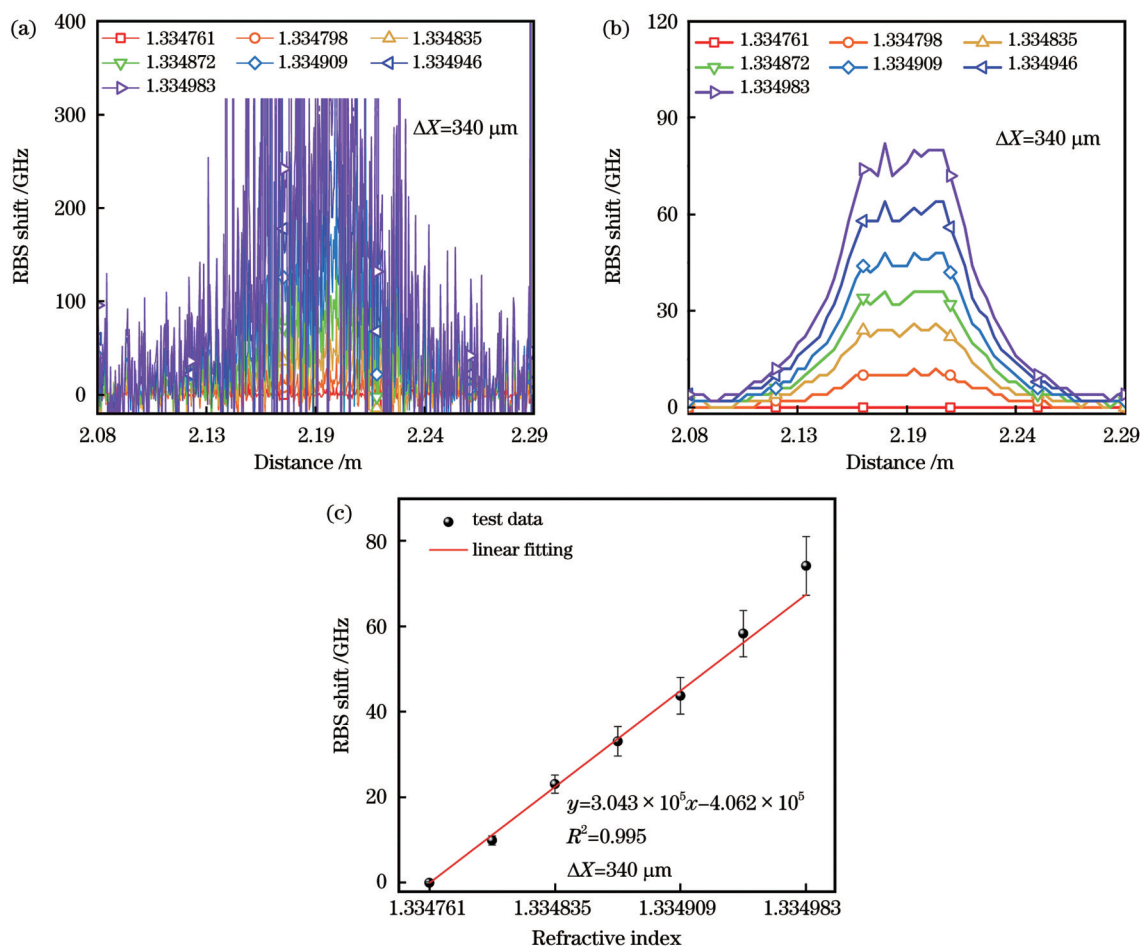


图 7 拉锥光纤传感区域 RBS 移动随距离的变化。(a)传感空间分辨率为 340 μm 时不同折射率下 RBS 随距离的变化;(b)传感空间分辨率为 340 μm 时不同折射率下 RBS 随距离的变化;

Fig. 7 RBS shifts changed with distance in the tapered fiber sensing region. (a) RBS shifts as functions of distance at different RI when $\Delta X=340 \mu\text{m}$; (b) RBS shifts as functions of distance at different RI when $\Delta X=340 \mu\text{m}$; (c) linear fitting result between RBS shift and RI when $\Delta X=340 \mu\text{m}$

5 结 论

利用拉锥光纤传感器,提出一种基于OFDR差分相位解调方式的分布式折射率传感方法。首先,理论分析了差分相位折射率传感原理并仿真计算了相位随外界折射率变化的灵敏度特性。在实验中,实现了在340 μm传感空间分辨率下的分布式折射率传感。通过对有效传感区域相位变化以及外界折射率变化进行线性拟合,验证了相位和外界折射率变化有着良好的线性度,其线性拟合度为0.997,各折射率下的最大标准差为0.0067 rad,平滑后的测量灵敏度为1328.6 rad/RIU,与仿真结果1483.7 rad/RIU接近。更重要的是,与传统互相关解调方法相比,差分相位解调方法的传感空间分辨率提升了10倍,且不同折射率下的线性拟合度与测量标准差均优于传统互相关解调方法。受到扫频范围的限制,本实验的传感空间分辨率 $\Delta Z=68 \mu\text{m}$,因此在 $H=5$ 下传感空间分辨率已经达到340 μm。理论上可以通过扩大扫频范围来提升系统的传感空间分辨率。然而,随着扫频范围的扩大,相位噪声增大。本文受限于SMF信噪比,因此选择小的扫频范围。如果未来使用更高信噪比的待测光纤,如拉锥光纤光栅,同时选择适当的扫频范围,那么基于差分相位法的分布式折射率传感有望实现几十微米甚至几微米传感空间分辨率下的感知,这为未来实现微米级分布式生物传感提供了思路。

参 考 文 献

- [1] Loyez M, DeRosa M C, Caucheteur C, et al. Overview and emerging trends in optical fiber aptasensing[J]. *Biosensors & Bioelectronics*, 2022, 196: 113694.
- [2] Wang X D, Wolfbeis O S. Fiber-optic chemical sensors and biosensors (2015-2019)[J]. *Analytical Chemistry*, 2020, 92(1): 397-430.
- [3] Wang X D, Wolfbeis O S. Fiber-optic chemical sensors and biosensors (2013-2015)[J]. *Analytical Chemistry*, 2016, 88(1): 203-227.
- [4] Liu L, Zheng J, Deng S J, et al. Parallel polished plastic optical fiber-based SPR sensor for simultaneous measurement of RI and temperature[J]. *IEEE Transactions on Instrumentation and Measurement*, 2021, 70: 9508308.
- [5] Spasopoulos D, Kaziannis S, Danakas S, et al. LSPR based optical fiber sensors treated with nanosecond laser irradiation for refractive index sensing[J]. *Sensors and Actuators B: Chemical*, 2018, 256: 359-366.
- [6] 蒙云清, 董贤, 武创, 等. 裸露纤芯边孔光纤布拉格光栅制备及其折射率传感特性研究[J]. 激光与光电子学进展, 2022, 59(1): 0106003.
Meng Y Q, Dong X, Wu C, et al. Fabrication and refractive index sensing characteristics of exposed-core side-hole fiber Bragg grating[J]. *Laser & Optoelectronics Progress*, 2022, 59(1): 0106003.
- [7] Qi L, Zhao C L, Yuan J Y, et al. Highly reflective long period fiber grating sensor and its application in refractive index sensing [J]. *Sensors and Actuators B: Chemical*, 2014, 193: 185-189.
- [8] Kim D C, Dunn R C. Integrating whispering gallery mode refractive index sensing with capillary electrophoresis separations using phase sensitive detection[J]. *Analytical Chemistry*, 2016, 88(2): 1426-1433.
- [9] Wang X, Wang S, Jiang J F, et al. High-accuracy hybrid fiber-optic Fabry-Pérot sensor based on MEMS for simultaneous gas refractive-index and temperature sensing[J]. *Optics Express*, 2019, 27(4): 4204-4215.
- [10] Qian W W, Chan C C, Zhao C L, et al. Photonic crystal fiber refractive index sensor based on a fiber Bragg grating demodulation[J]. *Sensors and Actuators B: Chemical*, 2012, 166/167: 761-765.
- [11] Luo H P, Sun Q Z, Li Y P, et al. Highly birefringent D-shaped microfiber and its application in high-sensitive optical sensing[J]. *IEEE Sensors Journal*, 2016, 16(12): 4793-4797.
- [12] Wang P F, Brambilla G, Ding M, et al. High-sensitivity, evanescent field refractometric sensor based on a tapered, multimode fiber interference[J]. *Optics Letters*, 2011, 36(12): 2233-2235.
- [13] 陈颖, 张敏, 丁志欣, 等. 基于全介质超表面的微流体折射率传感器[J]. 中国激光, 2022, 49(6): 0613001.
Chen Y, Zhang M, Ding Z X, et al. Microfluidic refractive index sensor based on all-dielectric metasurfaces[J]. *Chinese Journal of Lasers*, 2022, 49(6): 0613001.
- [14] 代小爽, 王双, 谭珂, 等. TiO₂纳米粒子增强的光纤损失模式共振折射率传感器[J]. 光学学报, 2023, 43(10): 1006003.
Dai X S, Wang S, Tan K, et al. Optical-fiber refractive index sensor based on lossy mode resonance enhanced by TiO₂ nanoparticles[J]. *Acta Optica Sinica*, 2023, 43(10): 1006003.
- [15] Froggatt M, Moore J. High-spatial-resolution distributed strain measurement in optical fiber with Rayleigh scatter[J]. *Applied Optics*, 1998, 37(10): 1735-1740.
- [16] Bao X Y, Chen L. Recent progress in distributed fiber optic sensors[J]. *Sensors*, 2012, 12(7): 8601-8639.
- [17] Du Y, Jothibasu S, Zhuang Y Y, et al. Rayleigh backscattering based macrobending single mode fiber for distributed refractive index sensing[J]. *Sensors and Actuators B: Chemical*, 2017, 248: 346-350.
- [18] Xu P B, Yu X F, Chen Z J, et al. Distributed refractive index sensing based on bending-induced multimodal interference and Rayleigh backscattering spectrum[J]. *Optics Express*, 2021, 29(14): 21530-21538.
- [19] Sypabekova M, Korganbayev S, Blanc W, et al. Fiber optic refractive index sensors through spectral detection of Rayleigh backscattering in a chemically etched MgO-based nanoparticle-doped fiber[J]. *Optics Letters*, 2018, 43(24): 5945-5948.
- [20] Zhu Z D, Ba D X, Liu L, et al. Temperature-compensated distributed refractive index sensor based on an etched multi-core fiber in optical frequency domain reflectometry[J]. *Optics Letters*, 2021, 46(17): 4308-4311.
- [21] Fu C L, Sui R L, Peng Z W, et al. Distributed refractive index sensing based on etched Ge-doped SMF in optical frequency domain reflectometry[J]. *Sensors*, 2023, 23(9): 4361.
- [22] Ji W B, Liu H H, Tjin S C, et al. Ultrahigh sensitivity refractive index sensor based on optical microfiber[J]. *IEEE Photonics Technology Letters*, 2012, 24(20): 1872-1874.
- [23] Ding Z Y, Sun K L, Liu K, et al. Distributed refractive index sensing based on tapered fibers in optical frequency domain reflectometry[J]. *Optics Express*, 2018, 26(10): 13042-13054.
- [24] Hua P D, Ding Z Y, Liu K, et al. Distributed optical fiber biosensor based on optical frequency domain reflectometry[J]. *Biosensors & Bioelectronics*, 2023, 228: 115184.
- [25] Gifford D K, Froggatt M E, Kreger S T. High precision, high sensitivity distributed displacement and temperature measurements using OFDR-based phase tracking[J]. *Proceedings of SPIE*, 2011, 7753: 77533I.
- [26] Gifford D K, Froggatt M E, Sang A K, et al. Multiple fiber loop strain rosettes in a single fiber using high resolution distributed sensing[J]. *IEEE Sensors Journal*, 2012, 12(1): 55-63.

- [27] Lin J P, Zhao M M, Tu G J, et al. The analysis and comparison of cross-correlation and phase demodulation methods in an OFDR system for strain/temperature sensing[J]. Proceedings of SPIE, 2018, 10821: 1082125.
- [28] Zhao S Y, Cui J W, Wu Z J, et al. Distributed fiber deformation measurement by high-accuracy phase detection in OFDR scheme [J]. Journal of Lightwave Technology, 2021, 39(12): 4101-4108.
- [29] Feng W, Wang M F, Jia H L, et al. High precision phase-OFDR scheme based on fading noise suppression[J]. Journal of Lightwave Technology, 2022, 40(3): 900-908.
- [30] Wang C H, Liu K, Ding Z Y, et al. High sensitivity distributed static strain sensing based on differential relative phase in optical frequency domain reflectometry[J]. Journal of Lightwave Technology, 2020, 38(20): 5825-5836.
- [31] Guo Z, Yan J Z, Han G C, et al. High-resolution φ -OFDR using phase unwrap and nonlinearity suppression[J]. Journal of Lightwave Technology, 2023, 41(9): 2885-2891.
- [32] Tur M, Boger Y S, Shaw H J. Polarization-induced fading in fiber-optic sensor arrays[J]. Journal of Lightwave Technology, 1995, 13(7): 1269-1276.
- [33] Lina J M, Mayrand M. Complex daubechies wavelets[J]. Applied and Computational Harmonic Analysis, 1995, 2(3): 219-229.
- [34] Kreger S T, Gifford D K, Froggatt M E, et al. High resolution distributed strain or temperature measurements in single- and multi-mode fiber using swept-wavelength interferometry[C] // Optical Fiber Sensors, October 23-27, 2006, Cancún, Mexico. Washington, DC: OSA, 2006: ThE42.

Distributed Refractive Index Sensing Based on Differential Phase in Optical Frequency Domain Reflectometry

Hua Peidong, Ding Zhenyang*, Liu Kun, Guo Haohan, Zhang Teng, Li Sheng, Liu Ji,
Jiang Junfeng, Liu Tiegen

School of Precision Instrument and Optoelectronics Engineering, Key Laboratory of the Ministry of Education on Optoelectronics Information Technology (Tianjin University), Tianjin Optical Fiber Sensing Engineering Center, Tianjin University, Tianjin 300072, China

Abstract

Objective Optical fiber refractive index (RI) sensors have caught widespread attention from researchers in biochemical sensing and environmental monitoring due to their high precision, high sensitivity, resistance to electromagnetic interference, corrosion resistance, low cost, and easy preparation. The commonly employed optical fiber RI sensors currently include surface plasmon resonance, local surface plasmon resonance, fiber Bragg gratings, long-period fiber Bragg gratings, fiber-optic whispering gallery mode, fiber Fabry-Perot sensors, photonic crystal fibers, D-type fibers, and tapered fibers. However, most fiber optic RI sensors are currently single-point sensors and cannot achieve multi-point detection or even distributed sensing. Based on the detection of Rayleigh backscattering spectra (RBS) in optical fiber, optical frequency domain reflectometry (OFDR) features high measurement accuracy, high sensing spatial resolution, and long measurement distance, which makes it very suitable for distributed RI sensing. Distributed RI sensing can not only obtain the RI magnitude in the solution but also locally detect the diffusion processing of the solution and test the distribution of fluids. These are all that single-point sensors or even quasi-distributed sensors cannot achieve.

Methods Traditional distributed RI sensing based on OFDR adopts a cross-correlation demodulation algorithm, which has sound noise suppression ability and stability. However, it is difficult to achieve distributed RI measurements with a micron-level spatial resolution. Therefore, this type of distributed RI sensing based on cross-correlation demodulation is not enough to be applied to distributed biological analysis, drug design, and other fields. Unlike cross-correlation demodulation methods, OFDR based on differential relative phase demodulation realizes sensing by the relative phase change of RBS. Since the differential phase demodulation method directly measures the relative phase change caused by external RI changes, this method is more sensitive than traditional cross-correlation demodulation methods. Therefore, the differential relative phase demodulation method is expected to achieve distributed RI sensing with a micron-level spatial resolution.

Results and Discussions We first theoretically analyze the principle of differential relative phase demodulation and the RI sensitivity characteristics. To characterize the theoretical sensitivity of the differential phase demodulation method and compare it with experimental results, we simulate the relationship between phase variation and external RI change at a taper waist of $6 \mu\text{m}$. The simulation results are shown in Fig. 1(a), and the slope of 1483.7 rad/RIU is the theoretical sensitivity. Meanwhile, in Eq. (11), Δf is related to taper waist radius r . Therefore, the relationship between theoretical

sensitivity and the diameter of the taper waist can be simulated, with the results shown in Fig. 1(b). In the experiment, the phase variations along distance in the sensing area of tapered fiber are compared when only average denoising and wavelet denoising are adopted. This reveals that only average denoising cannot achieve distributed RI sensing at the micron level. Meanwhile, with only wavelet denoising, the phase variations caused by the RI changes in the sensing region with a spatial resolution of $68 \mu\text{m}$ can be distinguished. However, due to the excessive phase noise in the subfigure of Fig. 5(b), there are still significant fluctuations in the demodulation signal of the sensing region. After average denoising ($H=5$) and wavelet denoising, phase fluctuation noise can be well suppressed with a sensing spatial resolution of $340 \mu\text{m}$. The phase variations along the fiber distance under different RI can be clearly distinguished. The results are shown in Fig. 6(c). A linear fitting curve between phase variations and the external RI change at the effective sensing region is shown in Fig. 6(d) with a linear fit of 0.997. The maximum standard deviation at each RI is 0.0067 rad, and the smoothed measurement sensitivity is 1328.6 rad/RIU, which is close to the simulation results in Fig. 1(b). To compare the difference between the proposed differential phase demodulation method and the traditional cross-correlation demodulation method, we utilize cross-correlation demodulation to the data in Fig. 6. The linear fitting curve of the proposed differential phase demodulation method is better than that of the cross-correlation algorithm. Meanwhile, the standard error of the smoothed differential phase demodulation method is lower than that of the cross-correlation demodulation algorithm. More importantly, compared to the cross-correlation demodulation method, the differential phase demodulation method increases the sensing spatial resolution by 10 times, reaching the level of hundreds of micrometers.

Conclusions We present distributed RI sensing by tapered fiber based on differential relative phase OFDR. The principle of the proposed method is theoretically analyzed and the sensitivity of phase variations with external RI changes are simulated. In the experiment, we achieve distributed RI sensing with a spatial resolution of $340 \mu\text{m}$ after average denoising and wavelet smoothing. The effective sensing area is 45 mm. The linear fitting between phase variations and external RI change is 0.997 and the maximum standard deviation at each RI is 0.0067 rad. The experimental RI sensitivity is 1328.6 rad/RIU, close to the simulation result of 1483.7 rad/RIU. The linear fitting and standard deviation of the differential phase method are better than those of the cross-correlation algorithm. More importantly, the sensing spatial resolution is improved by 10 times. The proposed differential relative phase method based on OFDR provides a foundation for achieving micrometer-level distributed biosensing.

Key words fiber optics; distributed optical fiber sensing; refractive index sensing; optical frequency domain reflectometry; differential phase demodulation; tapered fiber